IOPscience iopscience.iop.org

Home Search Collections Journals About Contact us My IOPscience

Overview of results from the MST reversed field pinch experiment

This content has been downloaded from IOPscience. Please scroll down to see the full text.

2013 Nucl. Fusion 53 104017

(http://iopscience.iop.org/0029-5515/53/10/104017)

View the table of contents for this issue, or go to the journal homepage for more

Download details:

IP Address: 128.104.165.63
This content was downloaded on 26/09/2013 at 15:57

Please note that terms and conditions apply.

IOP Publishing and International Atomic Energy Agency Nuclear Fusion
Nucl. Fusion **53** (2013) 104017 (7pp) doi:10.1088/0029-5515/53/10/104017

Overview of results from the MST reversed field pinch experiment

J.S. Sarff[1], A.F. Almagri[1], J.K. Anderson[1], M. Borchardt[1], D. Carmody[1], K. Caspary[1], B.E. Chapman[1], D.J. Den Hartog[1], J. Duff[1], S. Eilerman[1], A. Falkowski[1], C.B. Forest[1], J.A. Goetz[1], D.J. Holly[1], J.-H. Kim[1], J. King[1], J. Ko[1], J. Koliner[1], S. Kumar[1], J.D. Lee[1], D. Liu[1], R. Magee[1], K.J. McCollam[1], M. McGarry[1], V.V. Mirnov[1], M.D. Nornberg[1], P.D. Nonn[1], S.P. Oliva[1], E. Parke[1], J.A. Reusch[1], J.P. Sauppe[1], A. Seltzman[1], C.R. Sovinec[1], H. Stephens[1], D. Stone[1], D. Theucks[1], M. Thomas[1], J. Triana[1], P.W. Terry[1], J. Waksman[1], W.F. Bergerson[2], D.L. Brower[2], W.X. Ding[2], L. Lin[2], D.R. Demers[3], P. Fimognari[3], J. Titus[4], F. Auriemma[5], S. Cappello[5], P. Franz[5], P. Innocente[5], R. Lorenzini[5], E. Martines[5], B. Momo[5], P. Piovesan[5], M. Puiatti[5], M. Spolaore[5], D. Terranova[5], P. Zanca[5], V. Belykh[6], V.I. Davydenko[6], P. Deichuli[6], A.A. Ivanov[6], S. Polosatkin[6], N.V. Stupishin[6], D. Spong[7], D. Craig[8], R.W. Harvey[9], M. Cianciosa[10] and J.D. Hanson[10]

[1] University of Wisconsin, Madison, Wisconsin, USA and the Center for Magnetic Self-Organization in Laboratory and Astrophysical Plasmas
[2] Physics Department, The University of California at Los Angeles, Los Angeles, CA, USA
[3] Xantho Technologies, LLC, Madison, WI, USA
[4] Physics Department, Florida A&M University, Tallahassee, FL, USA
[5] Consorzio RFX, Associazione EURATOM-ENEA sulla Fusione, Padova, Italy
[6] Budker Institute of Nuclear Physics, Novosibirsk, Russia
[7] The Oak Ridge National Laboratory, Oak Ridge, TN, USA
[8] Physics Department, Wheaton College, Wheaton, IL, USA
[9] CompX, Del Mar, CA, USA
[10] Physics Department, Auburn University, Auburn, AL, USA

E-mail: jssarff@wisc.edu

Received 13 December 2012, accepted for publication 19 March 2013
Published 26 September 2013
Online at stacks.iop.org/NF/53/104017

Abstract
An overview of recent results from the MST programme on physics important for the advancement of the reversed field pinch (RFP) as well as for improved understanding of toroidal magnetic confinement more generally is reported. Evidence for the classical confinement of ions in the RFP is provided by analysis of impurity ions and energetic ions created by 1 MW neutral beam injection (NBI). The first appearance of energetic-particle-driven modes by NBI in a RFP plasma is described. MST plasmas robustly access the quasi-single-helicity state that has commonalities to the stellarator and 'snake' formation in tokamaks. In MST the dominant mode grows to 8% of the axisymmetric field strength, while the remaining modes are reduced. Predictive capability for tearing mode behaviour has been improved through nonlinear, 3D, resistive magnetohydrodynamic computation using the measured resistivity profile and Lundquist number, which reproduces the sawtooth cycle dynamics. Experimental evidence and computational analysis indicates two-fluid effects, e.g., Hall physics and gyro-viscosity, are needed to understand the coupling of parallel momentum transport and current profile relaxation. Large Reynolds and Maxwell stresses, plus separately measured kinetic stress, indicate an intricate momentum balance and a possible origin for MST's intrinsic plasma rotation. Gyrokinetic analysis indicates that micro-tearing modes can be unstable at high beta, with a critical gradient for the electron temperature that is larger than for tokamak plasmas by roughly the aspect ratio.

(Some figures may appear in colour only in the online journal)

© 2013 IAEA, Vienna Printed in the UK & the USA

1. Introduction

This paper provides an overview of recent results from the MST reversed field pinch (RFP) programme, summarizing physics important for the advancement of the RFP as well as for improved understanding of toroidal magnetic confinement in general. Topics covered include confinement physics, energetic particle effects, 3D helical equilibria, momentum transport, and magnetic self-organization physics. The MST is a large RFP device ($R = 1.5$ m, $a = 0.5$ m) that operates at medium plasma current ($I_p < 0.6$ MA). The RFP magnetic configuration offers several potential advantages for fusion as a result of the concentration of magnetic field within the plasma, including the possibility for normal magnets, a high particle density limit, and ohmic heating to burning plasma conditions. Unlike configurations with large toroidal field, the magnetic field strength in the RFP is minimum at the magnets. These features promote a fusion power vision for high power density and high reliability through the use of relatively simple technology. For example, the possibility for ohmic heating implies that the boundary could be optimized for heat removal and particle control without interference from rf launching structures otherwise needed for auxiliary heating. In a more general context, the RFP's large magnetic shear and weaker toroidal effects complement the physics regimes of tokamak and stellarator plasmas. Hence RFP research helps advance the predictive capability of fusion plasma science by exploring parameter ranges that would otherwise be inaccessible.

2. Classical ion confinement in the RFP

Evidence for the classical confinement of ions in the RFP is shown by (1) analysis of impurity ion transport in improved-confinement plasmas obtained with inductive current profile control and (2) energetic ion studies using 1 MW neutral beam injection (NBI). Each of these results is described in turn in the subsections below. We first summarize two paths to improved confinement in the RFP that have emerged in recent years. Fluctuation-induced (anomalous) transport in the RFP has typically been dominated by parallel losses in the stochastic magnetic field associated with magnetohydrodynamics (MHD) tearing instabilities that create a broad spectrum of modes. This mutli-helicity regime is represented in figure 1 by the shape of an outer flux surface, which is complex and distorted as a result of kink and tearing instability. (The degree of distortion is magnified ten-fold for illustration purposes.) The path on the left illustrates self-organization of the RFP plasma towards the single-helicity regime, where one mode dominates plasma dynamics and the remaining secondary modes are reduced in amplitude. This path has been significantly advanced by the RFX-mod programme as the plasma current has been increased to its 2 MA design value. New results from MST in this area of research are described in section 3. The path on the right in figure 1 illustrates the approach to tearing stability using profile control. Previous research on MST has shown that inductive pulsed parallel current drive (PPCD) greatly reduces magnetic fluctuations associated with tearing modes, yielding a ten-fold increase in the global energy and particle confinement times [1]. Under these conditions, the confinement quality in the RFP is similar to that for a same-size, same-current tokamak plasma [2].

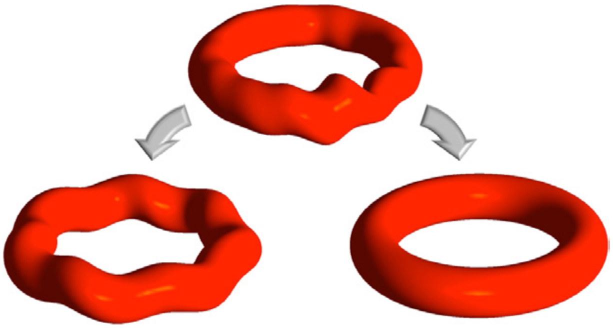

Figure 1. Two pathways for improved confinement in the RFP: quasi-single-helicity self-organization (left) and profile control for kink/tearing stability (right). The distortion of the toroidal plasma shape is magnified for illustration purposes.

2.1. Impurity ion confinement

The RFP is unlike the tokamak and stellarator configurations in that the gradient in $|\boldsymbol{B}|$ is almost normal to magnetic surfaces, everywhere on a surface. The magnetic connection length is also shorter, since $B_p \sim B_t$. The drift of particle guiding centres off a magnetic surface is therefore small, e.g., the banana orbit width for trapped particles is less than their gyro-radius. For perpendicular collisional transport, the irreducible limit in the RFP is thus classical, not neoclassical, despite the fraction of trapped particles being about the same as for a tokamak configuration with the same aspect ratio. With PPCD, the test-particle diffusivity for ions in a stochastic magnetic field is reduced below the classical transport level. This creates an opportunity to observe the expected classical confinement, despite the RFP being a toroidal plasma.

Measurements of impurity ions obtained by charge-exchange recombination spectroscopy (CHERS) in PPCD plasmas have allowed a comparison of the experimental ion confinement with classical transport expectations [3, 4]. The radial profile of the fully stripped carbon density is measured to become hollow, as shown in figures 2 and 3, revealing outward particle convection and low particle transport. Modelling of the diffusion of impurity ions for classical transport agrees well with the measured carbon profile evolution, and temperature screening explains the hollow profile, expected when the temperature profile is more peaked than the density profile. The modelling is time dependent and includes collisional coupling between the dominant ion species in MST plasmas [3]. The comparison in figure 3 is made near the end of the improved-confinement period. The hollow profile is predicted to appear within 10 ms, due to the anti-pinching effect of the temperature screening mechanism. It is noteworthy that a tokamak plasma with the same density and temperature profiles as for MST plasmas but subject to neoclassical transport would be expected to have a peaked impurity ion density profile. (The impurity flux's dependence on the temperature gradient does not exhibit temperature screening for neoclassical transport in the collisionality regime of these experiments.) The observed hollow profile is thus a clear signature of classical transport in this case.

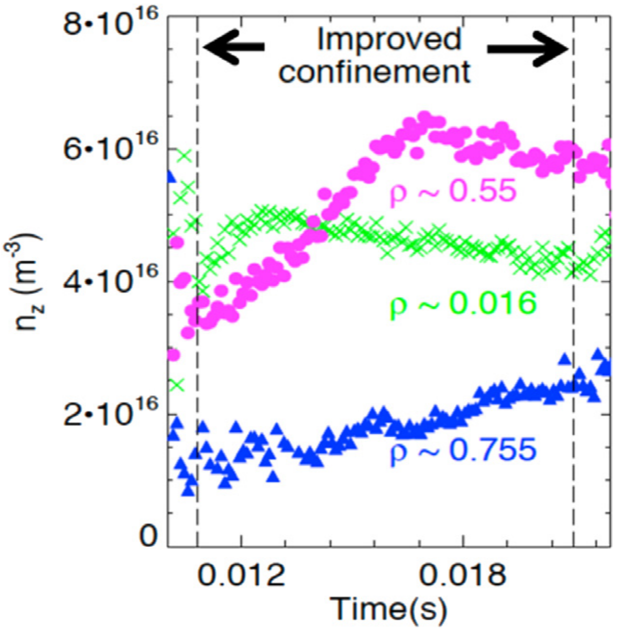

Figure 2. Evolution of the fully stripped carbon density during the PPCD improved-confinement phase measured at several radii, $\rho = r/a$.

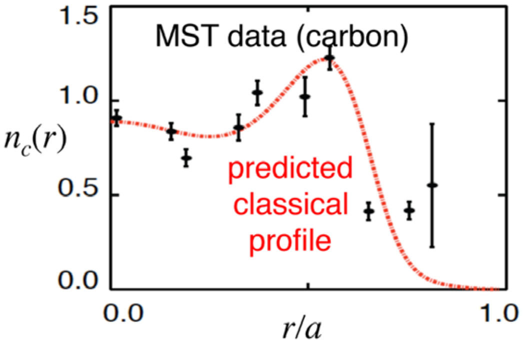

Figure 3. Radial profile of the carbon density measured using CHERS, compared with modelling for classical transport in the RFP.

2.2. Energetic ions from NBI

Classical confinement is also observed for energetic ions created by 1 MW, 25 keV NBI [4, 5]. The injector installed on MST is the first tangential NBI experiment performed in an RFP plasma [6]. (There is only one other high-power NBI experiment performed previously in an RFP, on the TPE-RX experiment [7].) The hydrogen beam is doped with 3% deuterium to observe the slowing-down of the fast-ion population via the decay of the d–d fusion neutron flux after sharp NBI turn-off as shown in figure 4, like the 'beam-blip' technique used in other experiments [8]. The measured characteristic neutron decay time can be separated as $\tau_{\text{n-exp}}^{-1} = \tau_{\text{n-classical}}^{-1} + \tau_{fi}^{-1}$, where $\tau_{\text{n-classical}}$ is the neutron flux decay resulting from the classical slowing-down of the beam-generated energetic ions, dominated by electron collisions. All other losses are represented by τ_{fi}, including those associated with charge-exchange and turbulence. Over a wide range of MST plasma conditions, the fast-ion confinement is close to classical, i.e., $\tau_{\text{n-exp}} \approx \tau_{\text{n-classical}}$, as shown in figure 5. In all cases, the fast-ion confinement time exceeds the thermal ion confinement time, $\tau_{\rm p} = 1$–10 ms. This is true even in standard RFP plasmas with large tearing instabilities that yield a stochastic magnetic field [9].

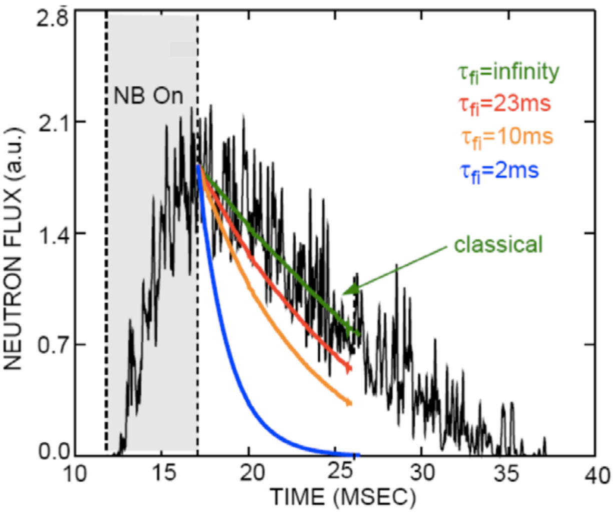

Figure 4. Neutron flux for short-pulse NBI. Several projections for varying τ_{fi} are shown, illustrating the fast-ion confinement is close to its classical expectation.

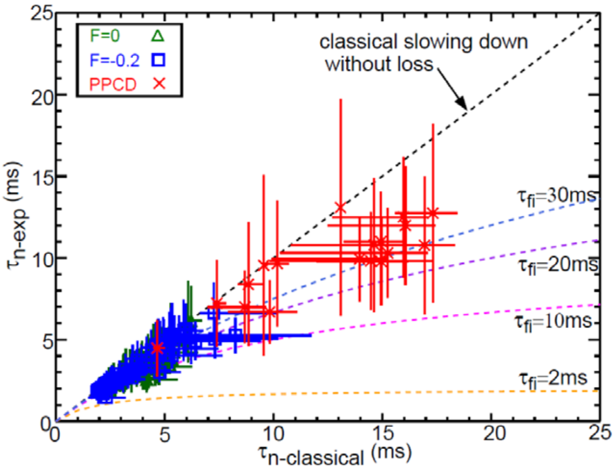

Figure 5. The measured neutron decay time versus the classical slowing-down time for a variety of MST plasma conditions. The reversal parameter, $F = B_{\rm T}(a)/\langle B_{\rm T}\rangle$, measures the degree of toroidal field reversal. Data shown for $F = 0$ and $F = -0.2$ represent a range of standard RFP operation. PPCD plasmas are hotter, with longer slowing-down times.

The energetic ions have super-Alfvénic speed and a strong density gradient in the core, stimulating the first appearance of fast-particle-driven modes by NBI in a RFP plasma [4, 10]. The tangential NBI geometry creates a fast-ion population localized to the core region, $r/a \lesssim 0.1$, with $v_{||} \gg v_{\perp}$ and $v_{fi}/v_{\rm A} > 1$. Using the NUBEAM module in TRANSP, the predicted local fast-ion density is 25% of the electron density in the absence of mode-induced transport or redistribution. However, the fast-ion density is yet to be directly measured, and there are indicators that the onset of the modes does in fact limit the fast-ion density [11]. Several modes are observed, one illustrated in figure 6, which shows a magnetic spectrogram for toroidal mode number $n = 5$ measured by a toroidal array of magnetic sensors at the plasma surface. The poloidal mode

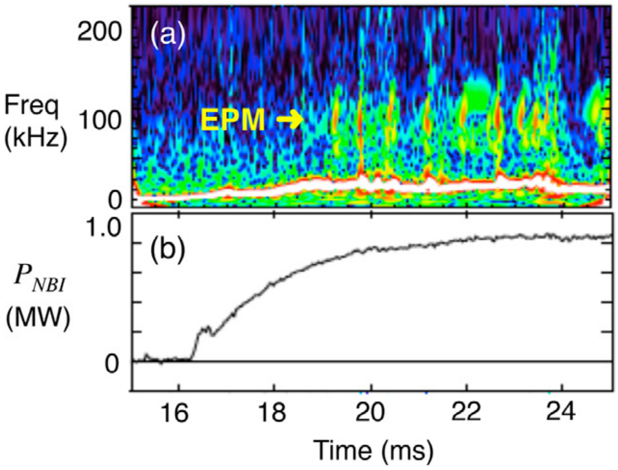

Figure 6. (*a*) Magnetic spectrogram for $n = 5$ and (*b*) the NBI power. The bright mode with $f \sim 20$ kHz is an $m = 1$ tearing mode resonant in the core.

number is dominantly $m = 1$. This mode and two others with $n = 4$ and $n = 1$ are bursty in character, appearing only with NBI. The $n = 5$ mode exhibits a scaling with the beam energy, with little dependence on the background plasma Alfvén speed. This mode is energetic-particle-like. The $n = 4$ mode exhibits scaling with the Alfvén velocity (magnetic field, density and ion mass varied), with weak dependence on the beam energy. While this is Alfvénic-like, both the $n = 4$ and $n = 5$ modes have frequencies smaller than expected for toroidal Alfvén eigenmodes that have been analysed using AE3D and STELLGAP [10]. The $n = 4$ mode (with Alfvénic-like scaling) is therefore speculated to be a resonant branch of the kinetic ballooning mode. MST's complement of advanced diagnostics is rapidly characterizing these modes, e.g., using FIR interferometry, scattering, and polarimetry that yield the radial profiles of the fluctuating density and magnetic field.

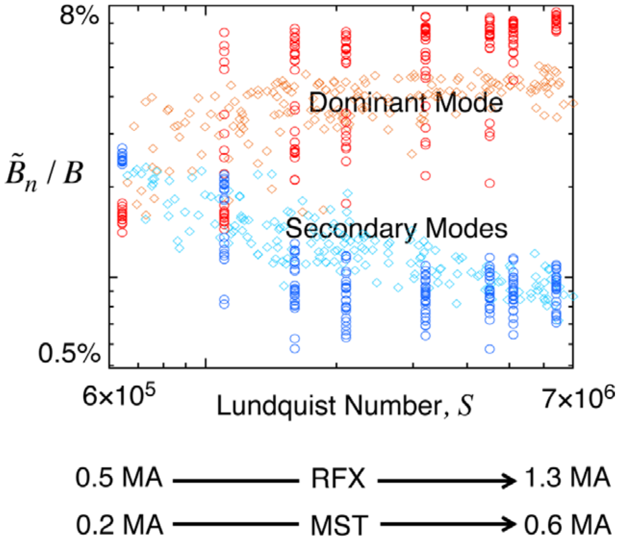

Figure 7. Magnetic fluctuation amplitude versus Lundquist number, S, for data from both RFX-mod (diamond symbol) and MST (circle symbol). The range of plasma current, I_p, for both experiments is noted. There are additional data from RFX-mod [15] extending to $S \sim 2 \times 10^7$ for $I_p \to 2$ MA that are not shown.

3. Quasi-single-helicity configuration

The quasi-single-helicity (QSH) state that forms spontaneously in RFP plasmas [12, 13] has commonalities to the stellarator and 'snake' formation [14] in tokamak plasmas. The QSH state is characterized by the growth of one toroidal mode in the tearing mode spectrum, while the other secondary modes are reduced. A helical structure within the plasma therefore becomes apparent. The strongest form of QSH appeared first in RFX-mod when plasma operations pushed to high current $I_p > 1$ MA and plasmas with a single helical magnetic axis formed, called the single-helical-axis (SHAx) configuration [15]. The SHAx configuration has now been formed in MST as well, notably with $I_p \sim 0.5$ MA, lower than the threshold for their appearance in RFX-mod. This apparent difference in current threshold, and the scaling for the QSH regime in general, may be better unified if there is a dependence on Lundquist number, $S = \tau_R/\tau_A = \mu_0 a V_A/\eta \sim I_p T_e^{3/2}/\sqrt{n}$, a key dimensionless parameter in MHD. The trends for magnetic fluctuation amplitudes versus S are shown in figure 7. The MST data are produced at lower density and higher temperature, and thus similar Lundquist number despite lower plasma current. As can be seen, the trends in the data from both MST and RFX-mod overlap when plotted versus S. The SHAx state in MST is accessible most robustly with shallow toroidal field reversal, which is also the typical operating regime for RFX-mod. This could indicate that limiting the appearance of $m = 0$ modes and commensurate nonlinear coupling to $m = 1$ modes may be key to long-lasting QSH periods. The dominant helical mode in MST has toroidal mode number $n = 5$ and grows as large as 8% of the axisymmetric field. The dominant mode in RFX-mod is $n = 7$, owing to its larger aspect ratio (yielding smaller safety factor). The secondary $m = 1$ modes, i.e., $n > 5$ (MST) or $n > 7$ (RFX-mod), decrease with increasing S. This implies reduced magnetic stochasticity. Measurements of the global energy confinement in MST show an improvement of ~50% with SHAx. If elements of current profile control are included, e.g., allowing the plasma current to slowly decay, the improvement in confinement is as large as three-fold in SHAx plasmas [12].

MST's substantial diagnostic set for profile measurements is well suited to advancing 3D equilibrium reconstruction methods. This work is proceeding using the V3FIT code, which is based on VMEC [16]. Existing diagnostics include multi-point Thomson scattering, FIR interferometry/polarimetry, CHERS, and Rutherford scattering. A new two-colour soft x-ray tomography system is near completion and will provide high time resolution reconstructions of the electron temperature in a poloidal plane. Previous work comparing 3D equilibrium modelling based on edge magnetics with data from the FIR system indicates that these diagnostics will be extremely valuable reconstruction constraints [17].

4. Predicting the sawtooth cycle and stochastic transport

The ability to perform computational modelling with parameters approaching those in experiments has improved through advances in computational resources. Nonlinear

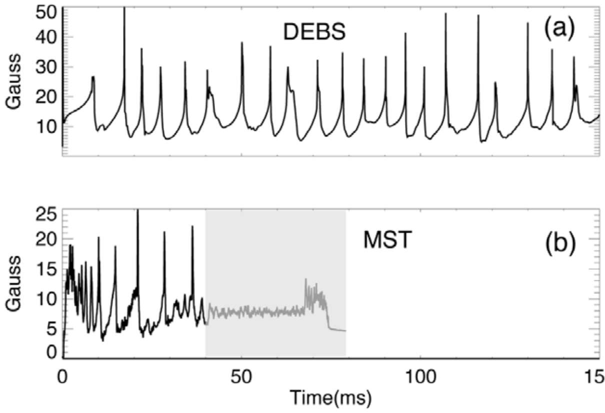

Figure 8. The rms amplitude of the m=1 magnetic fluctuations measured at $r = a$ in (a) the DEBS simulation and (b) MST experiment.

resistive MHD computation (DEBS code) with Lundquist number and resistivity profile matching MST standard RFP plasmas has been completed to investigate the tearing mode relaxation process [18, 19]. Such a comparison is valuable for validation efforts. The maximum Lundquist number for these calculations is $S = 4 \times 10^6$, and the magnetic Prandtl number, $P_m = \mu_0\nu/\eta$, is allowed to dynamically range from ∼250 between crashes to ∼3000 during the crash for numerical stability. The Prandtl number based on Braginskii coefficients for experimental parameters is $P_m \sim 1$, although the role of turbulent viscosity is unclear and would tend to increase the effective P_m. The calculation is also force-free, whereas the experimental standard RFP plasmas have poloidal $\beta_\theta \approx 5\%$. A finite pressure version of DEBS is also being used for these studies, but the results are too preliminary to report here. We note that earlier nonlinear resistive MHD computational studies of the RFP identified a relaxation–oscillation cycle, but these studies used a Lundquist number much less than for MST plasmas [20, 21].

A comparison of the rms magnetic fluctuation amplitude for $m = 1$ modes is shown in figure 8. The characteristic sawtooth relaxation cycle is evident in the fluctuation amplitude, with the simulation closely resembling the experimental behaviour. Other effects are also in good agreement but not shown here, such as the modification of the plasma current profile at the sawtooth crash. Note that the simulation is time-advanced for an effective pulse length of 150 ms, longer than the flattop portion of a single MST discharge. The greyed out portion of the MST waveform corresponds to the current ramp-down phase when the toroidal electric field is turned off, and hence the drive for current profile peaking and tearing instability is reduced. While the temporal dynamics of the sawtooth cycle are clearly similar, the fluctuation amplitude in the simulation is systematically about two times larger than measured in MST. The resolution of this difference may lie in effects beyond resistive MHD. For example, recent linear analysis of non-reduced MHD with the Hall term and gyro-viscosity shows that two-fluid effects tend to provide stability for the tearing modes [22]. This could possibly explain lower amplitudes in nonlinear saturation.

The DEBS simulations also provide a more refined representation of the magnetic field for evaluation and comparison of energy transport in a stochastic magnetic field [18, 19]. The magnetic diffusivity, $D_{\rm m}$, is evaluated directly from field line tracing using the DEBS mode spectrum, adjusted to match the experimental mode amplitudes measured at $r = a$. This is necessary since the predicted stochastic transport, $\chi_{\rm st} = v_{\rm th} D_{\rm m}$, is expected to scale strongly with the magnetic fluctuation amplitude as $D_{\rm m} \sim (\tilde{B}/B)^2$. Since the mode amplitudes are dynamic over the sawtooth cycle, this provides a stringent test of this scaling. The electron heat diffusivity was measured for the sawtooth cycle taking advantage of high-rep-rate lasers in MST's Thomson scattering diagnostic [23]. A comparison of the measured heat diffusivity, $\chi_{\rm e}$, with $\chi_{\rm e,st} = f_{\rm c} v_{\rm th,e} D_{\rm m}$, is shown in figure 9, where $f_{\rm c} \sim 0.5$ is the fraction of circulating electrons. The equilibrium field has a magnetic mirror associated with the toroidal geometry which leads to a trapped particle fraction comparable to that in a tokamak configuration of the same aspect ratio. This comparison is made in the mid-radius region of the plasma where the density of $m = 1$ resonant surfaces is high and the magnetic stochasticity is robust. The ∼2X reduction in $\chi_{\rm e,st}$ from particle trapping yields better agreement with measured $\chi_{\rm e}$.

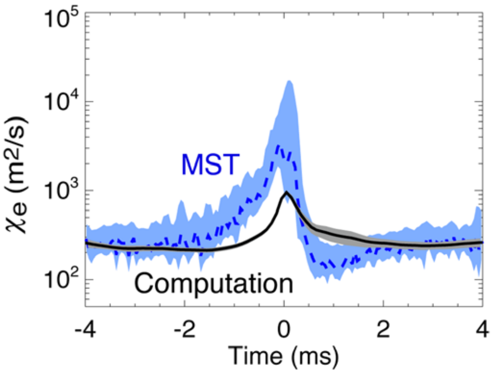

Figure 9. The electron heat conductivity during a sawtooth cycle (crash at $t = 0$) compared with the stochastic transport prediction.

5. Plasma flow and momentum transport

MST plasmas exhibit spontaneous plasma rotation, despite being ohmically heated. The flows are both perpendicular and parallel to the magnetic field, with the poloidal and toroidal components being similar in magnitude. This flow appears early on and dynamically varies during the sawtooth cycle. For example, the parallel flow profile peaks between sawtooth crash events, and then flattens during the crash. The sawtooth cycle for the flow in the core region is shown in figure 10. Previous MST measurements using probes in the edge and Faraday rotation in the core identified large Reynolds and Maxwell stresses associated with fluctuations at the tearing mode scale [24, 25]. The force densities from these stresses are enormous compared to the plasma inertia, but they tend to oppose each other. The spatially averaged correlation $\langle \tilde{\boldsymbol{J}} \times \tilde{\boldsymbol{B}} \rangle_{||}$ appears in the parallel Ohm's law as a Hall emf and in the parallel momentum balance as the Maxwell stress, so a coupling of electron and ion momentum processes during the relaxation process is exposed.

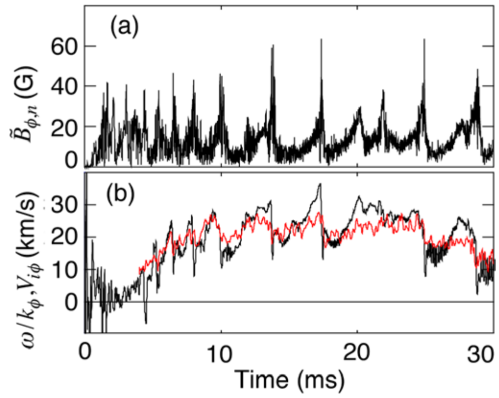

Figure 10. (*a*) The $n = 6$ magnetic fluctuation amplitude and (*b*) $n = 6$ toroidal phase velocity (black) and plasma flow (red).

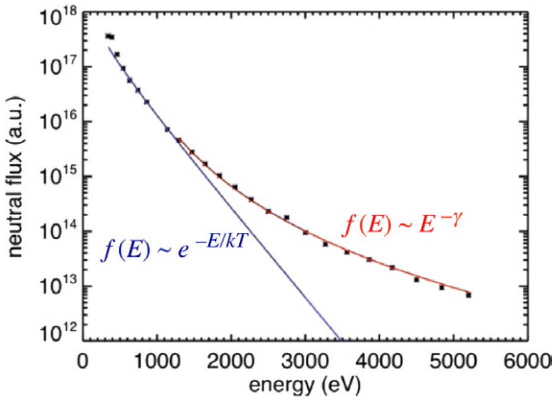

Figure 11. Neutral (deuterium) flux energy spectrum measured by the CNPA.

New work in this area includes (1) computational modelling using a non-reduced MHD model with two-fluid effects and (2) the experimental identification of a new turbulent stress associated with the correlation of plasma pressure and magnetic field fluctuations. The computational modelling is carried out using the NIMROD code with the inclusion of the Hall term in Ohm's law and gyro-viscosity in the momentum–density evolution [22, 26]. Similar to experimental observations, the force densities from the Reynolds and Maxwell stresses that appear in nonlinear multi-mode calculations tend to oppose each other. (The Hall term also produces a mean-field emf, $\langle \tilde{\boldsymbol{J}} \times \tilde{\boldsymbol{B}} \rangle_{||}/en_{\mathrm{e}}$, that is comparable in magnitude to $\langle \tilde{\boldsymbol{V}} \times \tilde{\boldsymbol{B}} \rangle_{||}$.) Thus a theoretical context to understand the coupled relaxation processes for current and momentum is emerging.

A new, separate fluctuation-induced stress has been measured that is associated with the correlation $\langle \tilde{p}_{||} \tilde{B}_r \rangle$ [27, 28]. This term is the heart of a 'kinetic stress' for parallel flow stemming from $\nabla \cdot \boldsymbol{P}$ in momentum balance. For measurement purposes, the pressure fluctuation is assumed separable as $\tilde{p}_{||} = T_{||}\tilde{n} + n\tilde{T}_{||}$, and an FIR interferometer–polarimeter is used to measure directly only the term $T_{||,\mathrm{i}} \langle \tilde{n} \tilde{B}_r \rangle$, using a Rutherford scattering diagnostic for the ion temperature measurement, T_{i}. While the magnitude of the kinetic stress is small compared to the Reynolds and Maxwell stresses described above, its force density is nevertheless comparable to the plasma inertia. It is also better resolved, in particular its magnitude between sawtooth crash relaxation events. The radial profile of the kinetic stress is directed to increase the parallel flow between sawtooth crash events, so it is important in the context of the spontaneous rotation of MST plasmas. The spontaneous rotation and momentum transport in magnetic relaxation thus involves an intricate balance of several fluctuation-induced stresses.

6. Non-collisional ion heating

Non-collisional ion heating is very powerful during the sawtooth crash phase, with the ion temperature reaching $T_{\mathrm{i}} \sim$ 2–3 keV. Several features of the heating process have been uncovered recently, including a majority ion mass dependence [29] and anisotropy [30], $T_\perp \geqslant T_{||}$ (measured in impurity ions using CHERS). Measurements of an apparent excess in d–d neutron flux implies that the ion distribution must not be Maxwellian. New compact neutral particle analyser (CNPA) measurements observe this energetic tail with a power-law energy dependence that is created spontaneously during the strong magnetic reconnection during the sawtooth crash [30]. This is shown in figure 11. Similar measurements in astrophysical plasmas with tails having a power-law distribution are common. The CNPA energy limit is 5 keV, but if the power-law is extrapolated to energy ~20 keV, the implied neutron flux is consistent with measurements. A second advanced NPA with higher energy range has recently been installed on MST, motivated by the 1 MW NBI experiments. Evidence for the energetic tail to at least 30 keV appears in ANPA's initial data.

7. Micro-turbulence in the RFP

Micro-turbulence from drift-wave-like instabilities might be important in the RFP when magnetic fluctuations are reduced. New gyrokinetic analysis indicates that micro-tearing modes can be unstable at high beta, with a critical gradient for the electron temperature that is larger than for tokamak plasmas by roughly the aspect ratio [31]. Ion-temperature-gradient (ITG) turbulence is unstable in MST-like discharges for $a/L_{\mathrm{T}} > 3$–4 at zero-β [32]. As β is increased, the ITG growth rate is reduced until a different instability becomes dominant in the growth rate spectrum for $\beta > 5\%$, as shown in figure 12. Finite beta stabilization of ITG occurs as in the tokamak, through coupling to shear Alfvén waves, and is controlled by the parameter $\mathrm{d}\beta/\mathrm{d}r$. The critical β for stabilization is higher in the RFP than for the tokamak by a factor proportional to the aspect ratio, a consequence of the smaller connection length in the RFP equilibrium. The mode that dominates instability above the critical β has a structure along the magnetic field line with odd parity in the electrostatic potential and even parity in the vector potential. This, and the mode frequency, identify the mode as micro-tearing. The mode has a temperature gradient threshold that is very close to that of ITG, with the growth rate rising more steeply than for the tokamak equilibrium as a/L_{T} increases above 3–4. This steep rise of growth with temperature gradient will produce profile stiffness in the temperature gradient. The micro-tearing growth rate is largest at moderate collisionality. Surprisingly, the

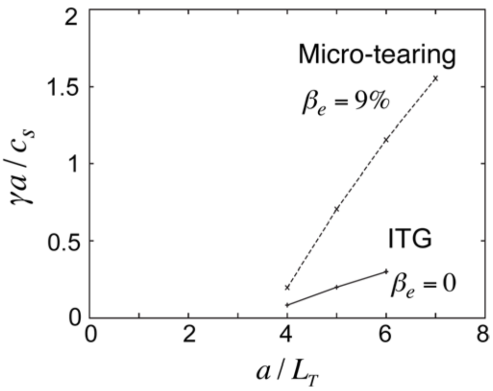

Figure 12. Linear growth rates of the most unstable modes versus the normalized temperature gradient scale length for $\beta = 0$ and 9%. The growth rate is normalized to c_s/a, where c_s is the sound speed and a is the minor radius.

growth rate remains significant even when the collisionality is small. The growth rate is sensitive to the curvature drift. The curvature drift frequency, which is neglected in tokamak micro-tearing theories, is larger in the RFP by a factor R/r. The larger value arises from the large poloidal field and its curvature scale length of radial displacement r. Variation of growth rate with curvature drift frequency, which is artificially modified in the code, behaves in a similar way to the magnetic-curvature drift-tearing instability [33]. Growth rates behave similarly across a wide range of collisionality, from the semi collisional regime to the collisionless limit, indicating that there is a collisionless branch of the instability not previously described. The MST experiment includes diagnostics such as fast Thomson scattering, FIR scattering, and a heavy ion beam probe that have the capability to identify micro-turbulence at these scales.

Acknowledgment

Work supported by US Department of Energy and National Science Foundation.

References

[1] Chapman B. *et al* 2009 *Nucl. Fusion* **49** 104020
[2] Sarff J. *et al* 2003 *Nucl. Fusion* **43** 1684
[3] Kumar S.T.A., Den Hartog D.J., Caspary K.J., Magee R.M., Mirnov V.V., Chapman B.E., Craig D., Fiksel G. and Sarff J.S. 2012 *Phys. Rev. Lett.* **108** 125006
[4] Anderson J. *et al* 2012 *Proc. 24th IAEA Fusion Energy Conf. (San Diego, CA, 2012)* (Vienna: IAEA) No EX/P3-16
[5] Anderson J.K. 2013 Fast ion confinement and stability in a neutral beam injected reversed field pinch *Phys. Plasmas* at press
[6] Anderson J.K. *et al* 2011 *Trans. Fusion Sci. Technol.* **59** 27
[7] Sakakita H., Kiyama S., Hirano Y., Yagi Y., Koguchi H., Shimada T., Sato Y. and Hayase K. *30th EPS Conf. on Controlled Fusion and Plasma Physics (St Petersburg, Russia, 2003)* (European Physical Society) vol 27A P-2.173 http://epsppd.epfl.ch/StPetersburg/PDF/ P2_173.pdf
[8] Heidbrink W., Kim J. and Groebner R. 1988 *Nucl. Fusion* **28** 1897
[9] Fiksel G., Hudson B., Den Hartog D.J., Magee R.M., O'Connell R., Prager S.C., Beklemishev A.D., Davydenko V.I., Ivanov A.A. and Tsidulko Y.A. 2005 *Phys. Rev. Lett.* **95** 125001
[10] Koliner J.J. *et al* 2012 *Phys. Rev. Lett.* **109** 115003
[11] Lin L. *et al* 2013 *Phys. Plasmas* **20** 030702
[12] Chapman B. *et al* 2012 *Proc. 24th IAEA Fusion Energy Conf. (San Diego, CA, 2012)* (Vienna: IAEA) No EX/P6-01 www-pub.iaea.org/iaeameetings/41985/24th-Fusion-Energy-Conference
[13] Martin P. *et al*, the MST Team, the EXTRAP Team and the TPE-RX Team 2003 *Nucl. Fusion* **43** 1855
[14] Cooper W., Graves J. and Sauter O. 2011 *Nucl. Fusion* **51** 072002
[15] Lorenzini R. *et al* 2009 *Nature Phys.* **5** 570
[16] Hanson J.D., Hirshman S.P., Knowlton S.F., Lao L.L., Lazarus E.A. and Shields J.M. 2009 *Nucl. Fusion* **49** 075031
[17] Bergerson W.F. *et al* 2011 *Phys. Rev. Lett.* **107** 255001
[18] Den Hartog D., Reusch J., Anderson J., Ebrahimi F., Forest C., Schnack D. and Stephens H. 2012 *Proc. 24th IAEA Fusion Energy Conf. (San Diego, CA, 2012)* (Vienna: IAEA) No EX/P3-17 www-pub.iaea.org/iaeameetings/41985/24th-Fusion-Energy-Conference
[19] Reusch J.A., Anderson J.K., Den Hartog D.J., Ebrahimi F., Schnack D.D., Stephens H.D. and Forest C.B. 2011 *Phys. Rev. Lett.* **107** 155002
[20] Kusano K. and Sato T. 1990 *Nucl. Fusion* **30** 2075
[21] Ho Y.L. and Craddock G.G. 1991 *Phys. Fluids B: Plasma Phys.* **3** 721
[22] King J.R., Sovinec C.R. and Mirnov V.V. 2012 *Phys. Plasmas* **19** 055905
[23] Den Hartog D.J. *et al* 2010 *Rev. Sci. Instrum.* **81** 10D513
[24] Ding W.X., Brower D.L., Craig D., Deng B.H., Fiksel G., Mirnov V., Prager S.C., Sarff J.S. and Svidzinski V. 2004 *Phys. Rev. Lett.* **93** 045002
[25] Kuritsyn A., Fiksel G., Almagri A.F., Brower D.L., Ding W.X., Miller M.C., Mirnov V.V., Prager S.C. and Sarff J.S. 2009 *Phys. Plasmas* **16** 055903
[26] Sovinec C., King J., Sauppe J., Mirnov V., Sarff J. and Ding W. 2012 *Proc. 24th IAEA Fusion Energy Conf. (San Diego, CA, 2012)* (Vienna: IAEA) No TH/P3-08 www-pub.iaea.org/iaeameetings/41985/24th-Fusion-Energy-Conference
[27] Ding W.X., Lin L., Brower D.L., Almagri A.F., Den Hartog D.J., Fiksel G. and Sarff J. 2012 *Proc. 24th IAEA Fusion Energy Conf. (San Diego, CA, 2012)* (Vienna: IAEA) No EX/P3-08 www-pub.iaea.org/iaeameetings/41985/24th-Fusion-Energy-Conference
[28] Ding W.X., Lin L., Brower D.L., Almagri A.F., Chapman B.E., Fiksel G., Den Hartog D.J. and Sarff J.S. 2013 *Phys. Rev. Lett.* **110** 065008
[29] Fiksel G., Almagri A.F., Chapman B.E., Mirnov V.V., Ren Y., Sarff J.S. and Terry P.W. 2009 *Phys. Rev. Lett.* **103** 145002
[30] Magee R.M., Den Hartog D.J., Kumar S.T.A., Almagri A.F., Chapman B.E., Fiksel G., Mirnov V.V., Mezonlin E.D. and Titus J.B. 2011 *Phys. Rev. Lett.* **107** 065005
[31] Carmody D., Terry P., Ren Y., Sarff J., Almagri A. and Pueschel M. 2012 *Proc. 24th IAEA Fusion Energy Conf. (San Diego, CA, 2012)* (Vienna: IAEA) No TH/P2-10 www-pub.iaea.org/iaeameetings/41985/24th-Fusion-Energy-Conference
[32] Tangri V., Terry P.W. and Waltz R.E. 2011 *Phys. Plasmas* **18** 052310
[33] Finn J.M. and Drake J.F. 1986 *Phys. Fluids* **29** 3672